CrystEngComm

ROYAL SOCIETY OF CHEMISTRY

PAPER

View Article Online
View Journal | View Issue

Cite this: *CrystEngComm*, 2020, **22**, 7204

Supramolecular organisation of sulphate salt hydrates exemplified with brucine sulphate†

Doris E. Braun

The solid form landscape of brucine sulphate (**BS**) was elucidated, resulting in three hydrate forms (**HyA**–**C**) and amorphous **BS**. Interconversion of the hydrates of **BS** with small changes in the relative humidity complicated identifying and characterising the solid forms. The hydrate obtained from crystallisation experiments (from water), **HyA**, is the only solid form described in the literature. The other two hydrates were produced by dehydration starting from the known hydrate. **HyA** contains 6.5 to 7.4 molecules of water per **BS** and is only stable in the relative humidity (RH) range ≥26% at room temperature (RT). **HyB** is only observable in a very narrow RH window (22–25%) at RT and shows a hexahydrate stoichiometry. At RH values ≤20%, the third hydrate, **HyC**, forms. Similar to **HyA**, the latter hydrate shows a variable water content of five or less water molecules per **BS**. Removal of the essential water molecules stabilising the hydrate structures causes the collapse to the amorphous state, a process which was not completed within 3.5 years of storing **HyC** under driest conditions (approx. 0%) at room temperature. Only the combination of intermolecular interaction and electronic structure calculations with thermal analytical techniques, X-ray diffraction, IR spectroscopy and gravimetric moisture (de)sorption studies and careful control of the external conditions allowed the discovery and rationalisation of the three hydrates of **BS**. The investigations on **BS** were complemented with an exploitation of the Cambridge Structural Database (CSD) to unravel the incidence of hydrates of sulphate salts. The analysis indicates that 56.5% of the sulphate salts (C, H, N, O, and S atoms only) are hydrate structures, with higher hydrates being more commonly present amongst sulphate salts than amongst all organic hydrates.

Received 6th November 2019,
Accepted 9th January 2020

DOI: 10.1039/c9ce01762c

rsc.li/crystengcomm

1. Introduction

It is well-known that a given organic compound can exist in more than one solid form. These various solid forms, polymorphs, solvates, hydrates or amorphous forms, may coexist under the same pressure and temperature conditions, and they normally show different physicochemical properties.[1–3] Control of solid forms is, therefore, of importance to any fine chemical industry, since solid forms provide a means to alter the properties of a product, without changing the molecule involved. Thus, screening for solid forms is an integral part in the development of (pharmaceutical) products and normally every newly developed compound is subjected to extensive crystal form screening in order to discover as many of the experimentally accessible polymorphs and solvates.[4–6] The optimum solid form properties, such as stability, solubility, dissolution rate and processability, may be engineered through considering single- or multicomponent crystals and amorphous forms.[7,8]

Solvent molecules from the crystallisation process can be included in the crystal lattice, leading to hydrates in the case of incorporated water and solvates for any other solvent. Hydrate formation among drug molecules is extremely common.[9–11] Since water is involved in many processing steps (*e.g.* wet granulation and freeze-drying) or can simply interact with the compound *via* atmospheric humidity, the existence of a hydrate and its phase stability must be known. For instance, the frequency of hydrate formation was found to be 38% for industrially screened compounds (n = 245)[10] and 34% for a database collection comprising the available literature for the organic compounds present in the European Pharmacopoeia (n = 960).[11] The latter analysis also indicated that the highest probability of hydrate formation was found among bigger molecules, hydrophilic substances and salts.

Hydrates (solvates) tend to crystallise more easily than solvent-free forms because of their often more efficient packing together with solvent molecules. The latter can be related to the two main structural reasons for solvate formation: (i) unsatisfied intermolecular interactions,

Institute of Pharmacy, University of Innsbruck, Innrain 52c, 6020 Innsbruck, Austria. E-mail: doris.braun@uibk.ac.at; Tel: +43 (0)512 507 58652

† Electronic supplementary information (ESI) available: Long-time dehydration experiments (PXRD data), Crystal Explorer calculations (**HyA**), moisture dependent PXRD measurements, and computational dehydration modelling. See DOI: 10.1039/c9ce01762c

compensated by the incorporation of solvent molecules, typically an imbalance between hydrogen-bonding donor and hydrogen-bonding acceptor groups in the molecule and (ii) solvent molecule inclusion in the crystal decreases the void space, thus leading to a more efficient packing. Most solvates (hydrates) include contributions from both driving forces.

Hydrates (solvates in general) can be grouped into stoichiometric and nonstoichiometric. For stoichiometric hydrates (solvates), with a precise and defined molecular ratio between the water and host in the crystal lattice, the water may play a crucial role in stabilising the network and therefore the loss of water (dehydration) results in a distinct crystal form (lower hydrate, neat or amorphous form).[12,13] In contrast, nonstoichiometric hydrates show a continuously variable composition within a certain RH range that is not associated with a significant change in the crystal lattice. It can even be possible to remove the entire hydrate water and retain the same crystal structure (isomorphic dehydrate), as for example seen for dapsone 0.33-hydrate[14] or brucine dihydrate.[15] The fact that water molecules can enter and leave the crystal lattice determined by the environmental RH conditions presents issues and challenges for formulating and storing (drug) products.

The stability of a hydrate (solvate) in general is determined by its crystal structure[16,17] and depends on the temperature and water activity it is exposed to.[18,19] Common techniques used to elucidate hydrate stability and its dehydration behaviour are thermal analytical methods and gravimetric moisture sorption/desorption experiments. Furthermore, computational methods can also be used to investigate the stability of hydrates (solvates),[20] their dehydration behaviour,[21,22] and even to predict their formation.[23–27]

The key to understanding a solid form is often the knowledge of its crystal structure, as its 3D packing arrangement may provide an understanding of its phase stabilities, transformations, and physicochemical properties. Single crystal X-ray diffraction can be seen as the ultimate technique for determining the crystal structure, but the main limitation of this method is the requirement of a single crystal of suitable size, quality, and stability, which is not always feasible. Many crystalline solids can be obtained only as microcrystalline powders, for example, phases prepared by solid-state (de)solvation processes[28,29] and slurry bridging experiments (grinding).[30] Then powder X-ray diffraction (PXRD) becomes the first method of choice for structural analysis.

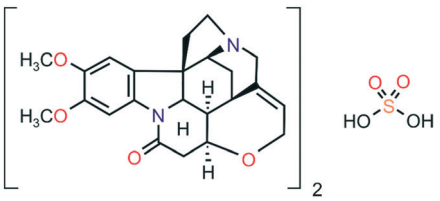

Fig. 1 Molecular diagram of brucine sulphate (**BS**).

In this study, brucine sulphate (**BS**, Fig. 1), was chosen as a model compound for detailed investigations of its hydration and dehydration behaviour.

The compound, an alkaloid, is a neurotoxin, which acts as an antagonist of glycine receptors. Brucine has been used for the treatment of liver cancer in Chinese medicine and additionally also its antiproliferative effects on different cancer cells have been reported.[31–35] However, the use of brucine as a treatment is limited due to its narrow therapeutic window. Furthermore, the alkaloid can be used as a tool for stereospecific chemical syntheses and as an enantioselective recognition agent in chiral resolution.[36–39] In contrast to the solid form landscape of brucine, which has been investigated thoroughly,[15,40–46] hardly any information can be found for the sulphate salt thereof. The structure of a heptahydrate has been determined in 2005.[47] However, no other information concerning solid forms or the stability of the hydrate can be found in the literature. This work surveys the solid form landscape of brucine sulphate, including the structural features, stabilities and interconversion pathways of two novel hydrate forms. State-of-the-art experimental methods, in combination with computational tools, were applied to provide a molecular understanding that describes the hydration/dehydration behaviour of the hydrates **HyA–C** and amorphous **BS**. To obtain a better understanding about hydrate formation and to unravel the frequency of hydrates among sulphate salts, the Cambridge Structural Database (CSD)[48] was consulted.

2. Materials and methods

2.1. Materials

Brucine sulphate (lot no. 236942684) was purchased from Fluka and consisted of the heptahydrate (**HyA**). The sample was used as obtained and transferred into hygrostats and equilibrated at 0% (over P_2O_5), 11% (saturated LiCl solution), 24% (KOAc), 43% (K_2CO_3) and 98% RH (K_2SO_4). Amorphous brucine sulphate was prepared by heating the hydrate (stored over P_2O_5) in a drying oven to 140 °C and keeping the temperature for 30 minutes.

2.2. Gravimetric moisture sorption/desorption analysis

Automated moisture sorption and desorption studies were performed with an automatic multisample gravimetric moisture sorption analyser SPS23-10μ (ProUmid, Ulm, D). The moisture sorption analyser was calibrated with saturated salt solutions according to the suppliers' recommendations. Approximately 100–160 mg of the sample was used for each analysis.

Samples of the amorphous form and the heptahydrate (**HyA**) of brucine sulphate were stored over P_2O_5 for one week prior to starting the gravimetric (de)sorption experiments. The measurement cycle for the two samples was started at 0% with an initial stepwise sorption process (increasing humidity) to 95%, followed by a desorption process (decreasing humidity) back to 0% relative humidity. RH changes were set to 5%. A second measurement was performed for **HyA** using a sample

pre-equilibrated over 43% RH (saturated K_2CO_3 solution). The second measurement cycle started at 43% RH with an initial stepwise desorption to 0%, followed by a sorption cycle back to 43% RH, with RH changes set to 2% (except for the step 43% ↔ 40% RH). The equilibrium conditions for each setup and step were set to a mass constant of ±0.001% over 60 minutes and a maximum time limit of 48 hours for each step.

In addition, manual water sorption/desorption studies were performed at 25 °C over a desiccant (P_2O_5). The loss of water as a function of time was determined gravimetrically[49] with a below-weighing balance (AT 250 semimicro balance, Mettler Instruments AG, Greifensee, CH). The sample mass used in these studies was about 200 mg.

2.3. Karl Fischer titration

Coulometric water determinations were performed using a Karl-Fischer-Titrator C20 (Mettler Toledo, Vienna, AT) and commercially available pyridine-free reagents.

2.4. Thermal analysis

For hot-stage thermomicroscopy (HSM) investigations, a Reichert Thermovar polarisation microscope, equipped with a Kofler hot-stage (Reichert, A), was used.

Differential scanning calorimetry (DSC) thermograms were recorded on a DSC 7 (Perkin-Elmer Norwalk, Ct., USA) controlled using the Pyris 2.0 software. Using a UM3 ultramicrobalance (Mettler, Greifensee, CH), samples of approximately 5 mg were weighed into perforated aluminium pans or high pressure capsules. The samples were heated using rates of 5 (perforated) of 10 (high pressure capsules) °C min^{-1} with dry nitrogen as the purge gas (purge: 20 mL min^{-1}). The instrument was calibrated for temperature with pure benzophenone (mp: 48.0 °C) and caffeine (236.2 °C), and the energy calibration was performed with indium (mp: 156.6 °C, heat of fusion: 28.45 J g^{-1}). The errors on the stated temperatures (extrapolated onset temperatures) and enthalpy values were calculated at the 95% confidence interval (CI) levels and are based on three measurements.

Thermogravimetric analysis (TGA) was carried out with a TGA7 system (Perkin-Elmer, Norwalk, CT, USA) using the Pyris 2.0 software. Approximately 5 mg of sample was weighed into a platinum pan. Two-point calibration of the temperature was performed with ferromagnetic materials (Alumel and Ni, Curie-point standards, Perkin-Elmer). A heating rate of 5 °C min^{-1} was applied and dry nitrogen was used as a purge gas (sample purge: 20 mL min^{-1}, balance purge: 40 mL min^{-1}). The errors on the stated mass losses were calculated at the 95% confidence interval (CI) levels and are based on at least three measurements.

2.5. Powder X-ray diffraction studies

PXRD patterns were obtained using an X'Pert PRO diffractometer (PANalytical, Almelo, NL) equipped with a θ/θ coupled goniometer in transmission geometry, a programmable XYZ stage with a well plate holder, a Cu $K\alpha_{1,2}$ radiation source with a focusing mirror, a 0.5° divergence slit, a 0.02° Soller slit collimator on the incident beam side, a 2 mm antiscattering slit, a 0.02° Soller slit collimator on the diffracted beam side and a solid state PIXcel detector. The patterns were recorded at a tube voltage of 40 kV and tube current of 40 mA, applying a step size of 2θ = 0.013° with 200 s or 600 s per step in the 2θ range between 2° and 40°. For non-ambient RH measurements, a VGI stage (VGI 2000M, Middlesex, UK) was used.

The diffraction patterns of **HyA** and **HyC** were indexed with DICVOL04 using the first twenty peaks and the space group was determined based on a statistical assessment of systematic absences,[50] as implemented using the DASH structure solution package.[51] Pawley fitting[52] was performed with Topas Academic V5.[53] The background was modelled with Chebyshev polynomials and the modified Thompson–Cox–Hastings pseudo-Voigt function was used for peak shape fitting.

2.6. Infrared spectroscopy

Infrared spectra were recorded with a temperature-controlled diamond ATR (PIKE GaldiATR) crystal on a Bruker Vertex 70 FTIR spectrometer (Bruker Analytische Messtechnik GmbH, Germany). The spectra were recorded between 4000 and 400 cm^{-1} at an instrument resolution of 2 cm^{-1} (38 scans per spectrum).

Principle component analysis (PCA), a multivariate data treatment to reduce the number of variables and provide a representation of the spectra in low dimensional space,[54–56] was used to interpret changes in the IR spectra of **BS** (hydrate and amorphous) during heating (dehydration). Spectra were pre-processed using min–max normalisation (Opus version 7.5, Bruker Optics, Ettlingen, Germany) and first derivatives were calculated using Simca-P (Version 11.0, Umetrics AB, Umeå, Sweden). The spectral region of 1725 to 400 cm^{-1} was used for constructing the PCA models.

2.7. Crystal Explorer calculations

The pairwise energy contributions to DAYRIF[47] (symmetry reduced to $P2_1$ to resolve the disorder, **HyA**) were calculated using Crystal Explorer V17.[57–59] The model energies were calculated between all unique nearest neighbour molecular pairs. The used model (termed CE-B3LYP) uses B3LYP/6-31G(d,p) molecular wave functions, calculated by applying the molecular geometries extracted from the crystal structures and Gaussian09.[60] This approach uses electron densities of unperturbed monomers to obtain four separate energy components: electrostatic (E_E), polarisation (E_P), dispersion (E_D), and exchange-repulsion (E_R). Each energy term was scaled independently to fit a large training set of B3LYP-D2/6-31G(d,p) counterpoise-corrected energies from both organic and inorganic crystals.[58]

2.8. Electronic structure calculations

The **HyA** (DAYRIF[47]) crystal structure was optimised *via* full periodic DFT-d simulations with the CASTEP (v.6.1) plane wave code[61] using the Perdew–Burke–Ernzerhof (PBE) generalised gradient approximation (GGA) exchange–correlation density functional[62] and ultrasoft pseudopotentials,[63] with the addition of a semi-empirical dispersion correction developed by Tkatchenko and Scheffler (TS)[64] and Grimme 06 (D2).[65] Brillouin zone integrations were performed on a symmetrised Monkhorst–Pack *k*-point grid with the number of *k*-points chosen to provide a maximum spacing of $2\pi \cdot 0.07$ Å^{-1} and a basis set cut-off of 560 eV. The self-consistent field convergence on total energy was set to 1×10^{-5} eV. Energy minimisations were performed using the Broyden–Fletcher–Goldfarb–Shanno optimisation scheme without space group constraints. The optimisations were considered complete when energies were converged to better than 2×10^{-5} eV per atom, atomic displacements converged to 1×10^{-3} Å, maximum forces to 5×10^{-2} eV Å^{-1}, and maximum stresses were converged to 1×10^{-1} GPa. To compute the isolated water energy (U_{gas}), DFT-d calculations were performed by placing a single molecule in a fixed $35 \times 35 \times 35$ Å^3 unit cell and optimised with the same settings as used for the crystal calculations.

Two models of a heptahydrate, seven models of a hexahydrate, six models of a pentahydrate and one model of a dehydrated **HyA** were prepared by systematically removing water molecules in the energy minimised **HyA** (symmetry reduced to $P2_1$) unit cell. All structures were fully optimised without any symmetry constraints. The resulting lower hydrated and anhydrous unit cells yielded slightly distorted cells compared to **HyA**. The crystallographic tool PLATON[66] was used to find the space group symmetry after unconstrained optimisations, resulting in either $C222_1$ or $P2_1$.

2.9. Cambridge Structural Database (CSD) analysis

The CSD (version 5.40 incl. updates 1–3)[48] was used for searching the error-free, polymer-free organic crystal structures ($C_{1-200}H_{1-200}N_{0-20}O_{0-20}S_{1-20}$) of sulphate salts. Duplicates, unreliable or incomplete structures and structures containing hydrogen sulphate were filtered out. This resulted in a set of 375 unique crystal structures.

3. Results and discussion

3.1. The solid form landscape of brucine sulphate

3.1.1. Thermal analysis of brucine sulphate hydrates. The TGA curves of the **BS** samples stored at distinct relative humidities (98%, 43%, 24% and 11%) are given in Fig. 2. Care was required to start the experiments immediately upon loading the samples, as the dry nitrogen purge alone was sufficient to induce dehydration at ambient temperatures. The measurements of the hydrate samples stored at 24%, 43% and 98% RH show a two-step mass loss upon heating. In contrast, the sample stored at 11% RH shows only a one-step mass loss thus, indicating that different hydrate phases of **BS** may exist. Furthermore, the TGA curves show that the higher the storage RH, the higher the mass loss (Table 1).

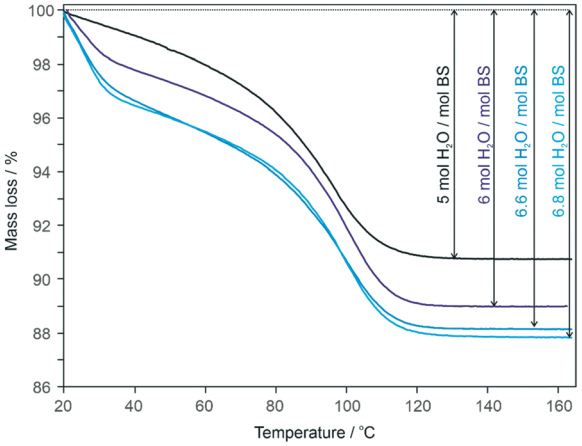

Fig. 2 Thermogravimetric analysis of the **BS** hydrate samples stored at 98%, 43%, 24% and 11% RH. The curves were recorded at a heating rate of 5 °C min^{-1}.

The **BS** hydrate stored at 98% shows a mass loss of 6.8 moles of water per mole **BS**, which is, considering the immediate mass loss upon exposure to dry conditions, in agreement with the heptahydrate stoichiometry reported in the literature.[40,47] The TGA curve of the sample stored at 43% RH shows a more or less identical dehydration course to that of the 98% RH sample.

Interestingly, the mass loss of the **BS** sample stored at 24% RH corresponded exactly to six moles of water per mole **BS** (Table 1). The course of the dehydration curve (TGA) is comparable with those of the 98% and 43% samples, but the curve shows a lower mass loss value. To clarify whether a distinct hydrate or a nonstoichiometric hydrate is present, orthogonal techniques were required under controlled humidity (see sections 3.1.3 & 3.1.5).

Finally, the sample stored at 11% RH shows a mass loss of five moles of water (pentahydrate) per mole **BS** during heating, lacking the first step compared to the three other samples but a similar course above 50 °C. Thus, it may be assumed that dehydration of the 98%, 43% and 24% samples proceeds *via* a pentahydrate. Dehydration is essentially completed at 130 °C under the conditions applied in the TGA experiments.

Table 1 Mass loss of the **BS** hydrate samples stored at distinct RHs and measured using TGA

Relative humidity/%	Mass loss/%	Mol H_2O/mol BS
98%	12.14 ± 0.05	6.80 ± 0.03
43%	11.83 ± 0.06	6.61 ± 0.04
24%	10.64 ± 0.61	6.03 ± 0.12
11%	9.22 ± <0.01	5.00 ± 0.01

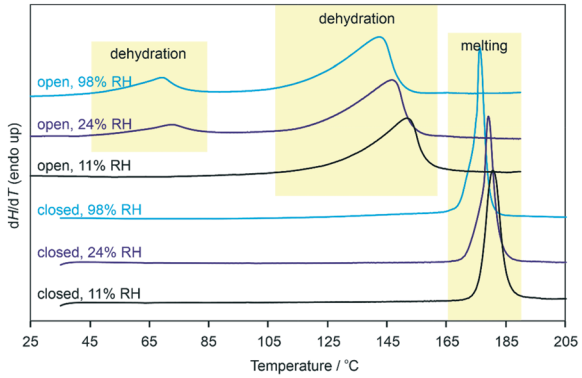

Fig. 3 DSC thermograms of the **BS** hydrate samples stored at 98%, 24% and 11% RH prior measurement. The curves were recorded either in 3-pinholed crucibles ('open') at a heating rate of 5 °C min^{-1} or in high-pressure DSC pans ('closed') at a heating rate of 10 °C min^{-1}.

The DSC curves (Fig. 3) recorded for the samples using 3-pinholed crucibles (perforated) mirror the events recorded in the TGA curves. Samples 98% and 24% (43% not shown) exhibit two dehydration endotherms in agreement with the two-step mass loss seen in the TGA curves, with the fist dehydration endotherm of the 24% sample showing a lower intensity than that of the 98% sample. This can be related to the fact that less water is released from the 24% sample. The 11% **BS** sample shows only one dehydration endotherm. Complete dehydration of the samples (>130 °C) resulted exclusively in amorphous **BS**.

The melting process of the hydrates stored under different RH conditions could be recorded using high-pressure DSC pans. The order of the melting temperature is inverse to that of the RH conditions where **BS** was stored, *i.e.* 174 °C, 175.5 °C and 176 °C for the 98%, 24% and 11% samples, respectively. All the hydrate samples had in common that only one melting process was observable. This is in contrast to the more complex DSC results seen for the brucine hydrate samples, where peritectic transformations into other hydrates and the anhydrate form were observed.[15] The high melting temperatures of the hydrates in a self-generated humid atmosphere (as produced in a hermetically sealed DSC container), testify their high stability.

3.1.2. Variable temperature IR spectroscopy and PCA. Variable temperature IR spectroscopy was employed to complement the DSC and TGA investigations. The IR spectra were recorded every 2 °C for the **BS** hydrate samples and amorphous **BS** from 25 to 190 °C, with the aim to map the dehydration pathways and potentially identify intermediate hydrate(s). The starting spectra (Fig. 4a) of the hydrate samples stored at different RHs exhibit very similar IR characteristics, differing mainly in peak intensities. A partial transformation of the higher to lower hydrates could not be prevented due to sample preparation and measurement conditions at ambient RH. Only amorphous **BS** exhibits clearly distinct IR bands compared to the hydrates.

Principal component analysis (PCA) was used to facilitate the analysis of the very similar IR spectra (Fig. 4b). Two

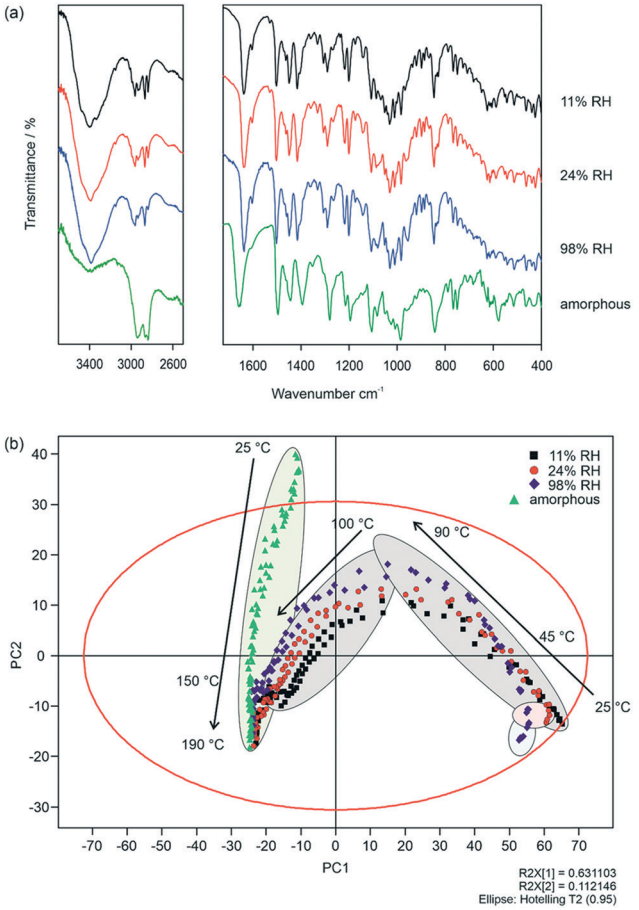

Fig. 4 (a) FT-IR spectra of amorphous **BS** and hydrates. (b) Plot of the first and second principal components (PC1 and PC2) from the principal component analysis of the IR spectra observed during heating of the amorphous and hydrated solid forms of **BS** from 25 to 190 °C. Each data point corresponds to an IR spectrum. Arrows highlight the two distinct transformation pathways. Distinct regions, corresponding to different solid-state forms, are highlighted. The red ellipse corresponds to the 95% Hotelling T^2.

distinct pathways are observed in the PC1 (principal component) *vs.* PC2 plot as the temperature increases. Amorphous **BS** follows an almost straight-line trajectory, with hardly any change in the PC1 value. This is in contrast to the course recorded for the other three samples. The three hydrate samples differ according to the TGA measurements in water content and slight differences are also indicated by the starting locations in the scores scatter plot. Upon increasing the temperature to approx. 45 °C, the points merge in location, which indicates that the higher hydrates pass through the lower hydrate. At temperatures above 90 °C, a directional change in the trajectory of the hydrates is observable, which can be attributed to a substantial change in the crystal structure. The latter corresponds to the dehydration of the pentahydrate (2nd dehydration process for the higher hydrates) as observed using thermal analytical techniques. At the end of the dehydration process, at approx. 150 °C, a second break of the trajectory is visible leading to the endpoint of the dehydration reaction where only

amorphous **BS** is present, as confirmed by the convergence of the two distinct pathways.

3.1.3. Gravimetric moisture sorption/desorption analysis of the brucine sulphate hydrates. To further investigate the possible hydration states of **BS**, the hydration and dehydration pathways were monitored as a function of RH at 25 °C. The experiments were started with the heptahydrate (**HyA** hereafter) and amorphous **BS** samples, which were equilibrated under driest conditions (over P_2O_5) for one week.

The hydrate sample (Fig. 5a) contained 3.8 moles of water per mole **BS** at the lowest RH conditions that could be reached in the automated (de)sorption analyser (<1% RH). Upon increasing the RH to 5%, a mass increase of one mole of water to a level of 4.8 moles of water per mole **BS** is observed, which only slightly increases to 5 moles by increasing the RH to 20%. On further increasing the RH, approx. one mole of water is sorbed at 25% RH and additional 0.5 moles at 30% RH (both values are in equilibrium). These distinct steps indicate that an intermediate hydrate exists (named **HyB**) in between the lower hydrate (**HyC**, ≤20% RH) and the higher hydrate (**HyA**, ≥30% RH). The water content of **HyA** was found to be variable, containing between 6.5 and 7.4 moles of water per mole **BS**. The sorption and desorption curves of the 5% step measurements do not show any hysteresis, indicating that the processes are perfectly reversible. With the exception of the ~0% RH values, **BS** shows fast (de)sorption kinetics.

Amorphous **BS** adsorbs up to 10 moles of water per mole **BS** before the mobility reaches a critical point, where the nucleation and growth of a crystalline phase occurs. The crystallisation process is accompanied by a release of excess water, indicated by the mass loss step between 70 and 75% RH in Fig. 5b. This behaviour is characteristic of amorphous samples of hydrophilic compounds, which can accommodate ("dissolve") much higher amounts of water than crystalline materials. The desorption curve in Fig. 5b follows the general course of that in Fig. 5a, although the intermediate step at 25% is not as pronounced as in the desorption curve of the hydrate sample. This suggests that the hydrate recrystallised from the amorphous phase shows a lower degree of order compared to the sample, which was already crystalline under the starting conditions.

To clarify whether the 25% point is really a distinct hydrate phase, a second, higher resolved moisture (de)sorption study was performed. The step size was reduced to 2% (Fig. 6), instead of 5% steps, and the measurement was performed only in the range between 43% RH (start) and 0% RH. The total change in the water content of **HyA** is about 0.3 moles of water per mole **BS** (molar ratio range: 6.5 to 6.8). Upon decreasing the RH from 26 to 24%, a distinct step is observable, indicating that an additional hydrate with six moles of water per mole **BS** exists (hexahydrate, **HyB**). The further humidity decrease induces a second step between 22% and 20% for the pentahydrate (**HyC**), which releases approx. 0.3 molecules of water per mole **BS** between 20% and 2%. A third step occurs then under the very driest conditions (<1% RH), where no equilibrium could be achieved within the measurement time (see the next section). A clear hysteresis is observable between the (de)sorption curves at the phase change step **HyA** ↔ **HyB**, which is characteristic of

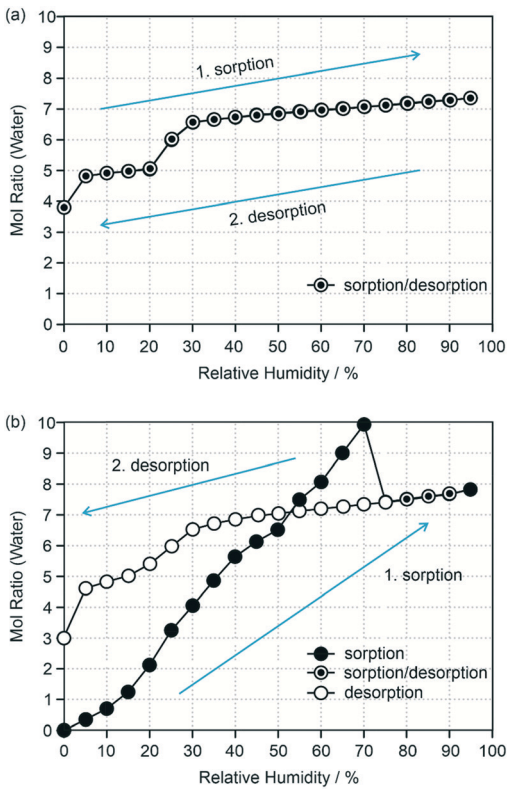

Fig. 5 Gravimetric moisture (de)sorption isotherms of (a) **BS** hydrate and (b) amorphous **BS**. The experiments were started at low RH values. The circles represent the data points, which, with the exception of the ~0% values (curves *a* and *b* desorption values), all fulfill the pre-set equilibrium conditions (see the Experimental section). Arrows indicate the direction of the experiment, *i.e.* sorption or desorption.

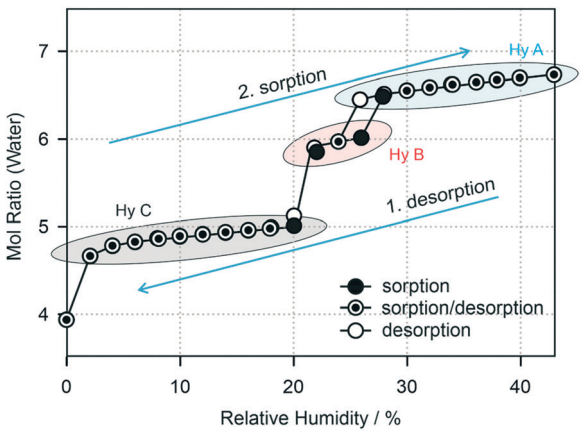

Fig. 6 Gravimetric moisture (de)sorption isotherms of **BS** hydrate. The experiments were started at 43% RH. The circles represent the data points. Arrows indicate the direction, *i.e.* sorption or desorption. Ellipses mark the existence ranges for each of the three **BS** hydrates.

a stoichiometric (de)hydration behaviour involving a discontinuous structural change.[12] Thus, **HyA** and **HyB** can be regarded as distinct hydrate phases. Also the distinct step between **HyC** and **HyB** is indicative of the presence of different hydrates. A hysteresis may be detectable if the step size is reduced to 1% (or below). Nevertheless, the narrow hysteresis range between **HyA**/**HyB** and **HyB**/**HyC** and fast transformation kinetics suggest that there is a strong structural resemblance between the hydrate phases, with structural rearrangements taking place beyond a simple nonstoichiometric (de)hydration reaction.

The step seen at a RH value <2% was further investigated in long-time storage experiments of the hydrate over P_2O_5 (~0% RH, Fig. 7). After ten days, the dehydration kinetics curve reached a plateau with a mole ratio of 1.5 moles of water per mole **BS**, accompanied with hardly any change in the PXRD pattern of **HyC** with a higher water content, apart from minor broadening of the peaks, indicating a slight loss of crystallinity. Over the next three years, the water content slowly decreased to less than one mole of water per mole **BS**. The intensity of the diffraction peaks decreased significantly and was found to be accompanied by anisotropic shifts to lower 2θ values, indicating that upon the loss of crystallinity the cell size increased slightly. Furthermore, the characteristic features of amorphous **BS**, amorphous halos, were visible (Fig. S1, ESI†). Upon exposure to moisture, a back-transformation to **BS** hydrate could be seen, likely triggered by the hydrate seeds still present in the sample. This is in contrast to the amorphous sample which did not transform back into a hydrate at ambient conditions.

It is possible to dehydrate **BS** hydrate at ~0% RH, however, the process will take years. The latter indicates that the water molecules are an essential part of the hydrate structures and strongly bound. Removal of the hydration water results in a structural collapse and amorphous **BS** is obtained.

3.1.4. Hydrate A – pairwise intermolecular energy calculations. The **HyA** structure of **BS**, solved by Bialonska and Ciunik,[47] crystallises in the orthorhombic $C222_1$ space group, with one brucinium, half a sulphate und 3.5 water molecules in the asymmetric unit. Thus, a heptahydrate

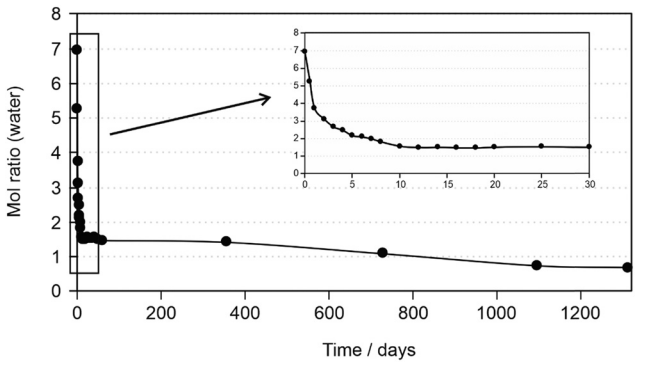

Fig. 7 Dehydration kinetics of **BS** hydrate at ~0% RH (over P_2O_5), monitored for 3.6 years.

stoichiometry is present. One water and the sulphate are located on special positions (2 axes). The brucinium cation adopts the same conformation, including the flexible methoxyl groups, as seen in all brucine structures.[24] Furthermore, the alkaloid features six hydrogen-bonding acceptor groups, but only one hydrogen-bonding donor group (N^+–H). The sulphate anion features only hydrogen-bonding acceptor groups. Thus, the incorporation of water molecules into the crystal structure allows the formation of strong hydrogen-bonding interactions in addition to the ionic interactions between the anion and cation. The hydrate structure can best be described as a layer structure, with one layer being formed by brucinium cations and the other by sulphate anions and water molecules (Fig. 8a). The layers are stacked in the direction of the *c* crystallographic axis and are held together through strong ionic interactions.

The four water molecules (W1 on a special position, W2, W3 and W4) are all capable of forming strong intermolecular interactions in **HyA**, with the classical strong hydrogen-bonding interactions being depicted in Fig. 8b. The strongest pairwise interactions are illustrated in the form of an energy framework[59] in Fig. 9 and all interactions involving water molecules are listed in Table S1, ESI.† The only (ionic) hydrogen bonding interaction formed not involving water is the N^+–H···O brucinium and sulphate interaction (not shown in Fig. 8b).

The strongest contributions to the **HyA** structure can be related to the ionic interactions (brucinium···sulphate, see Table S2, ESI†). Nevertheless, the pairwise intermolecular interactions involving the water molecules significantly contribute to the stability of the crystal lattice (Table S1, ESI†). Water W1 shows the weakest interaction energy in the **HyA** structure, followed by W3. The strongest interactions involving water molecules arise from the sulphate···water contacts, accounting for up to −128.9 kJ mol^{-1} in pairwise energy [for calculating the water intermolecular energies, the value has to be halved].

Interestingly, the strongest interaction involving W1 is not a classical strong hydrogen-bonding interaction, but a bifacturated C–H···O close contact, or weak hydrogen bonding interaction, as evident from the electrostatic contribution (Table S1, ESI†). The four strongest interactions involving W3 are between the water and sulphate, water and brucinium, and the two water···water interactions (Fig. 8b), with the brucinium interaction again being a weak hydrogen-bonding interaction. In the case of W4, two of the four strongest interactions arise from classical hydrogen-bonding interactions and two from brucine···water close contacts. Finally, for W2, with the water positions showing in sum the highest contributions to the intermolecular energy, the three strongest interactions arise from the three strong hydrogen-bonding interactions shown in Fig. 8b and do not involve the brucinium cation. Based on the CE-B3LYP energies, it might be concluded that W1 is the first water molecule to leave the **HyA** packing, followed by W3.

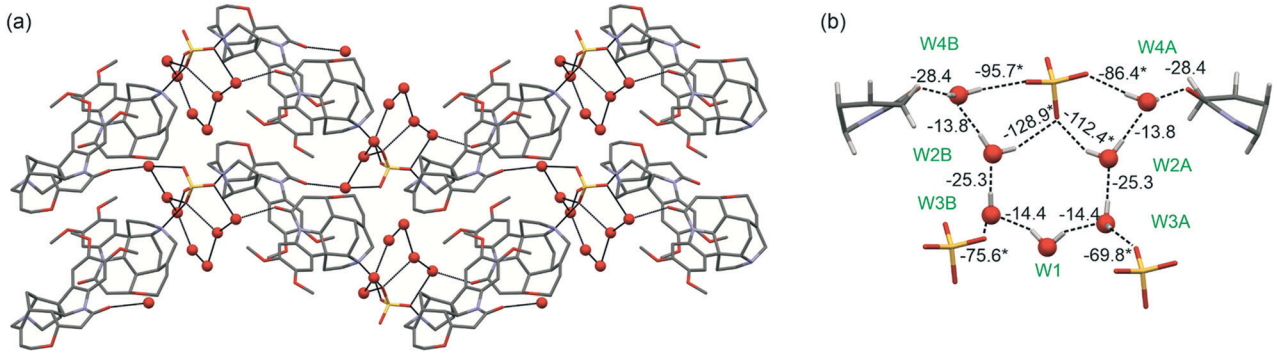

Fig. 8 (a) Packing diagram of **BS** heptahydrate (**HyA**) viewed along *ab*. For clarity, hydrogen atoms are omitted. Water oxygen atoms are shown as balls and only one of the sulphate molecule orientations is shown. Hydrogen-bonding interactions are depicted with black lines. (b) Strong hydrogen-bonding interactions involving water molecules in **HyA**: Water molecules are labelled in green and pairwise intermolecular energies are given. Values marked with "*" indicate that due to the different sulphate orientations differences in strength are observed. Note that only parts of the brucinium cations are shown for clarity.

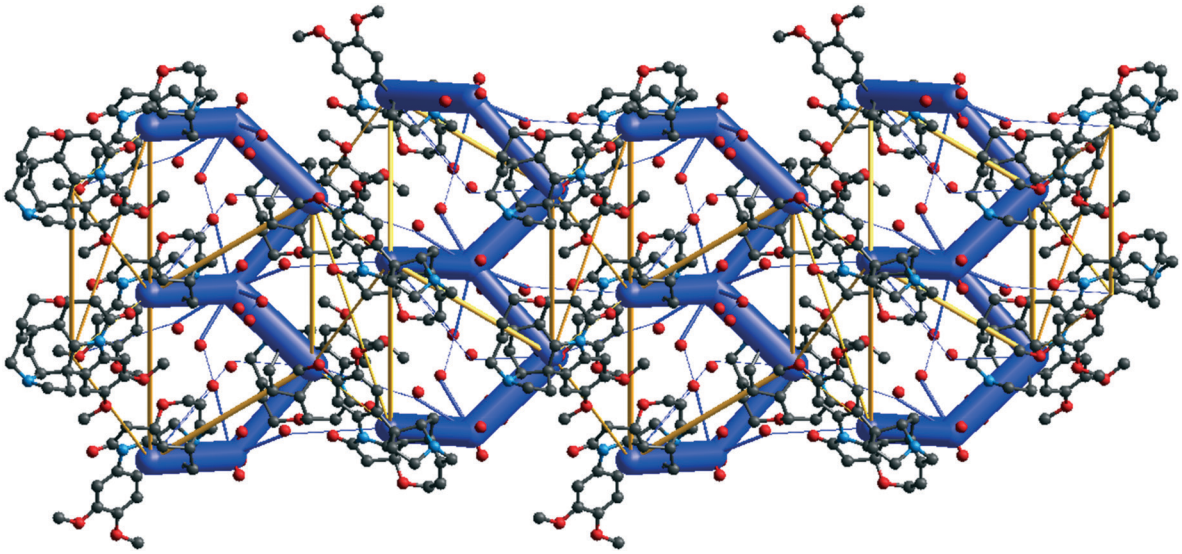

Fig. 9 Energy frameworks (total energy) for **HyA**. The energy scale factor is 10 and pairwise interaction energies with magnitudes smaller than 20 kJ mol^{-1} have been omitted. Stabilising and destabilising interactions are shown in blue and yellow, respectively.

3.1.5. Structural insights into the BS dehydration reaction. To investigate whether the three hydrates observed during the gravimetric moisture (de)sorption experiments show structural resemblance, the dehydration steps were correlated with structural changes observable using variable-humidity PXRD at 25 °C (Fig. 10). In agreement with the results obtained in Fig. 5a, distinct changes occur in the PXRD pattern of the hydrate sample at RH values <30% (Fig. 10a), confirming the presence of three distinct hydrates, with **HyC** and **HyA** clearly showing a higher structural resemblance than each of the latter two with **HyB** (Fig. 10b).

The (de)sorption data given in Fig. 10a confirm the reversibility of the dehydration and hydration processes, *i.e.* **HyA** ↔ **HyB** ↔ **HyC**. The RH dependent PXRD studies were repeated using a smaller step size with which the RH was reduced (Fig. S2, ESI†). Pawley fitting was used to estimate the change of the cell volume of **HyA** within the RH range of 90 to 26%, which corresponds to a change of 0.84 moles of water per mole **BS**. The latter was estimated to correspond only to 1.38% in cell volume (Table S2, ESI†). Overall, **HyA** can accommodate 6.5 to 7.4 moles of water per mole **BS** (26 to 90% RH), without a change in the crystal form. The latter implies that variability of water positions is required, compared to the solved heptahydrate structure,[47] to accommodate the additional 0.4 moles of water. Furthermore, the course of the gravimetric moisture (de)sorption data and the fact that indexing resulted in the same space group with only minor changes in the lattice parameters confirm that **HyA** shows a nonstoichiometric (de)hydration behaviour, but only in the RH range of 95 to 26% RH, *i.e.* **HyA** is a variable hydrate with respect to water content.

Further removal of hydration water results in a change of the diffraction pattern (Fig. 10). The latter hydrate, **HyB**, can be described as an intermediate phase, which can exist only within a very narrow RH range at RT. The change from **HyA**

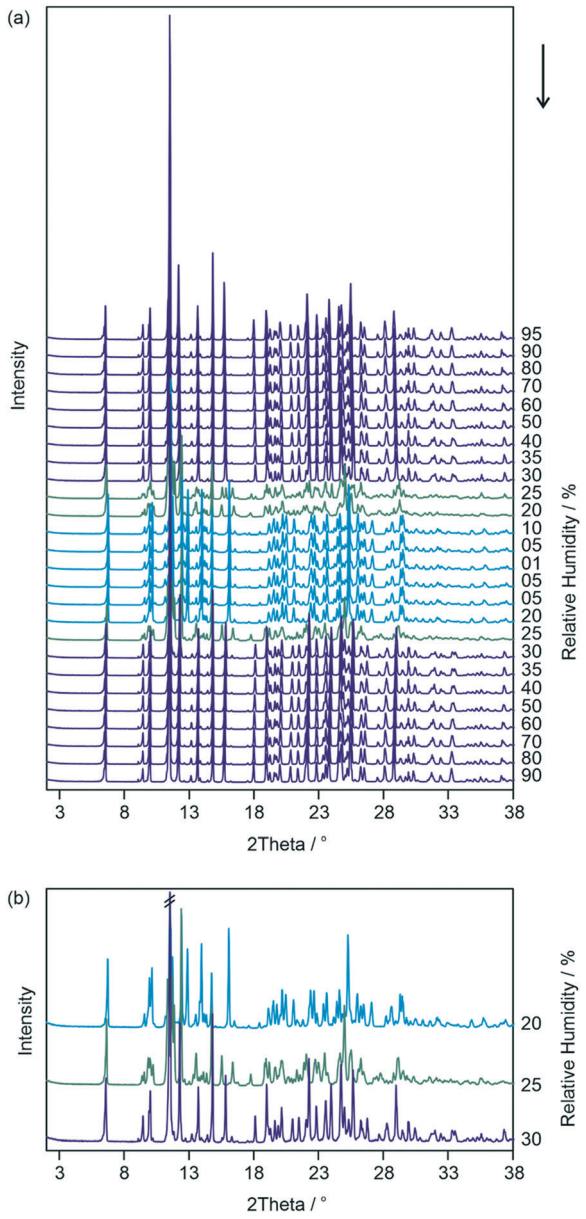

Fig. 10 (a and b) Moisture-dependent PXRD measurements of **BS** hydrates, indicating three different hydrates. The numbers given correspond to the RH in % at which the PXRD pattern was recorded.

to **HyB** involves a change in the crystal lattice, *i.e.* the patterns recorded for **HyB** cannot be indexed using the **HyA** lattice parameters allowing for changes in cell parameters which could be due to a change in the cell volume. Thus, the dehydration step from **HyA** to **HyB** and *vice versa* corresponds to a stoichiometric behaviour, which is also evident from the hysteresis seen in the sorption/desorption data. In contrast to **HyA**, the second hydrate (**HyB**) shows hardly any variance in the water content, which was estimated to be within 0.16 moles of water per mole **BS**, *i.e.* 5.85 to 6.01 moles of water. Thus, the upper limit of the hydration water of **HyB** is six moles of water per mole **BS**, in agreement with the mass loss measured in the TGA experiments.

A second change of the crystal form can be seen upon reducing the RH from 22 to 20%, which corresponds to a second reversible stoichiometric dehydration behaviour (**HyB** ⟷ **HyC**). It was possible to index the **HyC** pattern [$P2_1$, a = 9.494(1) Å, b = 26.088(3) Å, c = 9.298(1) Å, β = 98.111(3)°, V = 2279.94(32) Å^3, recorded at 18% RH]. For details, see Table S3, ESI.† The latter can be related to **HyA** (symmetry reduced from $C222_1$ to $P2_1$): a = 9.373 Å, b = 26.649 Å, c = 12.177 Å, β = 130.5°. Based on the gravimetric moisture (de)sorption experiments and RH controlled PXRD measurements, the water content changed by 1.07 moles of water per mole **BS** and 0.56% in cell volume, respectively, for **HyC**. Between four and five moles of water were present in **HyC**. As seen from the long-time experiments of **BS** at approx. 0% RH, more water can be removed; however, no other hydrate or anhydrate form is observable upon dehydrating **HyC**. Complete dehydration results in amorphous **BS**. The change in volume from **HyA** (26% RH) to **HyC** (18% RH), approx. 1.5 moles of water, was calculated to be 2.93%. Similar to **HyA**, **HyC** is a hydrate with a variable water content.

3.1.6. Computational dehydration modelling of HyA. The pairwise intermolecular energy calculations (section 3.1.4), based on the **HyA** structure, were complemented with periodic electronic structure calculations (DFT-d) starting from the optimised (and due to disorder symmetry reduced) hydrate structure. Systematically removing each of the seven **HyA** water molecules, followed by full structure optimisation, indicated that the most stable hexahydrate arrangement, starting from the **HyA** cell and therefore related to the structure, corresponds to the structure whose W3B water molecule had been removed (Fig. 11b). The second most stable arrangement was found if W3A was removed (Fig. 11c), *i.e.* 3.6 to 8.6 kJ mol^{-1}, less stable than if W3B was removed. Surprisingly, the removal of W1, which was earlier found to be the most weakly bound water position in **HyA** (Table S1, ESI†), leads to a packing arrangement which is already over 10 kJ mol^{-1} (Fig. 11a) less stable than the most stable computed hexahydrates. The different stability results with respect to the Crystal Explorer calculations are not surprising, as molecules were allowed to rearrange to increase their intermolecular energy contributions during the removal of the water molecules in the second set of calculations. By removing more than one water position a few relatively stable hexahydrate packing arrangements are obtained, which are all isostructural with **HyA**. In other words, none of the six computationally generated hexahydrate structures corresponds to **HyB**, which confirms that the **HyA** to **HyB** dehydration mechanism does not follow a nonstoichiometric route. This is also evident from the PXRD data (see the previous section).

Starting from the computationally generated lowest energy hexahydrate structure (Fig. 11b) and systematically removing each of the six water molecules, five of the pentahydrate structures were found to lie within approx. 15 kJ mol^{-1} of the lowest energy structure (Fig. 11d–h). Interestingly, the lattice

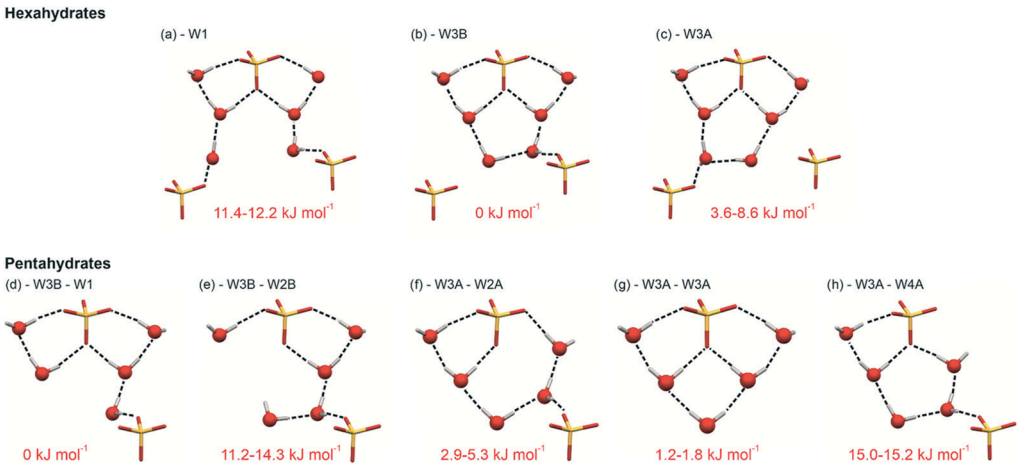

Fig. 11 Potential water molecule arrangements of **BS** (a–c) hexahydrate and (d–h) pentahydrate structures, with the **HyA** structure used as a starting point. Only hydrogen bonding interactions involving the water molecules are shown. Energy values correspond to lattice energy differences with respect to the most stable packing arrangement.

parameters and space group symmetry ($P2_1$) agree reasonably well with the values derived from indexing the **HyC** powder pattern, allowing anisotropic changes due to thermal effects, *i.e.* 0 K calculations and finite temperature PXRD measurements. Based on the small energy differences between some of the hypothetical pentahydrate structures, which are in the magnitude of the error of the applied method, it is likely that **HyC** corresponds to a mixture of packing arrangements depicted in Fig. 11d–h, in particular Fig. 11d, f and g. The latter also supports the fact that **HyC** can show a variable water content. Thus, water positions are likely to be partially occupied and more than one position can be missing in **HyC**. The average energy contribution of each of the water molecules present in the three most stable computed pentahydrates was estimated to be −74 to −81.5 kJ mol^{-1} and the values are in agreement with previous calculations on organic hydrates.[29,67]

An isomorphic dehydrate structure can be generated computationally by removing all of the water molecules from **HyA** (or **HyC**). The loss of the entire hydrate water was calculated as corresponding to a loss of −83.8 to −86.5 kJ mol^{-1} per water molecule, which is −6.5 to −9.6 kJ mol^{-1} per water molecule higher than that for the **HyA** to **HyC** transformation. This indicates that an isomorphic dehydrate structure would be extremely unstable and therefore unlikely to be observed experimentally. This is in agreement with the experimental dehydration behaviour. A closer inspection of the isomorphic dehydrate structure reveals void space which is sufficiently large to incorporate water molecules into the structure (Fig. 12). The isomorphic dehydrate structure cannot form a dense packing arrangement without water molecules, which is again in agreement with the fact that the removal of the essential hydrate water results in amorphous **BS** and not an isomorphic dehydrate.

3.2. Prevalence of hydrate formation among sulphate salts

A CSD analysis was performed to obtain insight into the prevalence of the hydrate formation of sulphate salt hydrates. The CSD (version 5.40) contained 375 unique structures of (small) organic sulphate salts (for details see section 2.9). The set of structures was analysed with respect to hydrate formation and hydrate stoichiometry, *i.e.* moles of water per mole sulphate. Overall, 56.5% of the sulphate structures contain water (Fig. 13a). Out of the remaining 43.5% of the structures, approx. 10% have a solvent molecule incorporated into the crystal lattice, *i.e.* salt solvates, with methanol and ethanol being the dominant solvent molecules. Only 39.2% of the structures are anhydrous (water-free and solvent-free) phases. The proportion of hydrate structures among sulphate salts is many times higher than the proportion of water containing structures of all organic compounds in the CSD, which was reported to be about 8% by Clarke *et al.* in 2010.[68] Thus, it is obvious that sulphate salts appear to be prone to hydrate formation. The percentage value derived in

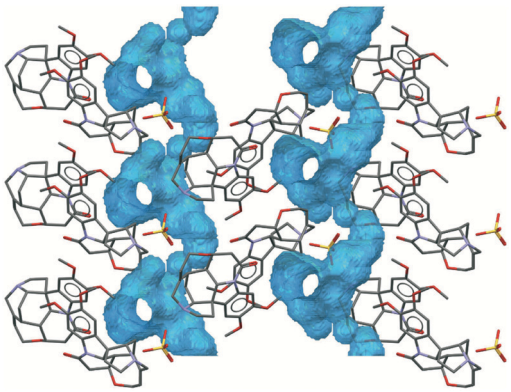

Fig. 12 Isomorphic **BS** dehydrate structure. The void (water) space was estimated using a 1.0 Å probe radius and a grid spacing of approx. 0.15 Å, using the Hydrate Analyser tool in Mercury.

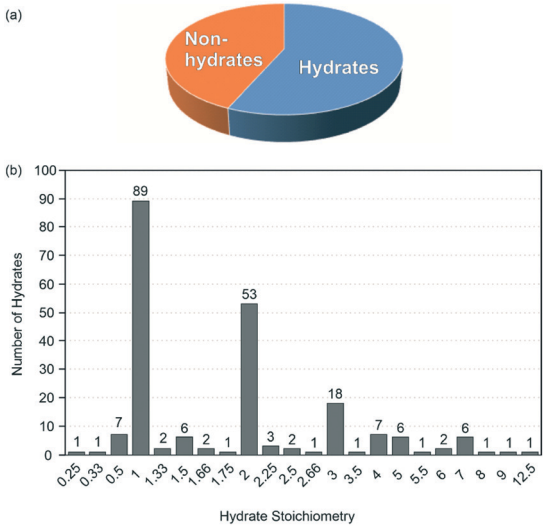

Fig. 13 Statistical analysis of the CSD (version 5.40 incl. updates 1–3) of organic sulphate structures with respect to (a) hydrate formation and (b) hydrate stoichiometry (water molecules per sulphate anion).

this study agrees well with literature findings comprising the drug molecules of the European Pharmacopeia, which revealed that 58.3% of the sulphate salts form at least one hydrate.[11]

The sulphate salt hydrate structures were grouped according to their molar water to sulphate ratio. In agreement with the overall analysis of hydrate structures,[69] monohydrates are by far the most common, followed by di- and trihydrates. An analysis by van de Streek and Motherwell showed that there is a definite tendency for higher molecular weight molecules to have a higher hydrate water content. The number of possible donor and acceptor atoms per structure also increases with a higher water content.[70] Interestingly, sulphate hydrates tend to include higher amounts of water compared to other hydrate forming compounds, with 11.8% of the sulphate hydrates containing at least four water molecules (Fig. 13b). Furthermore, it is also noteworthy that non-integer water ratios occur relatively frequently, either due to a unit cell containing one water molecule and two sulphate anions or due to the location of (salt) molecules on special positions.

The 25 higher hydrate structures, *i.e.* tetra- to 12.5-hydrates, were chosen for further analyses. The set of structures spans a molar mass range of 244.4 to 1705.9 g mol^{-1} (excluding water molecules). The average molar mass was found to be 633.3 g mol^{-1}, which is higher than the average found for small organic pharmaceuticals. A comparison with analyses concerning the frequency of hydrate formation, industrially screened compounds (n = 245)[10] and a database collection comprising the available literature for the organic compounds present in the European Pharmacopoeia (n = 960),[11,71] suggests that there is a greater tendency for hydrates to form with higher molecular weight molecules and with increasing number of polar groups and ionic charge. These observations are in agreement with the high incidence rate of hydrate formation among sulphate salts, *i.e.* due to the presence of ionic charges and bigger molecules (cations).

A bigger molecule is often also accompanied with the presence of more polar groups which tend to form strong hydrogen-bonding interactions in the crystal structure. van de Streek and Motherwell concluded in their statistical analysis of the CSD that crystal structures can cope with relatively high numbers of unsatisfied hydrogen-bond acceptors, but unsatisfied hydrogen-bond donors are highly unfavourable.[70] Statistical analyses of nearly 1000 pharmaceuticals indicate that the probability of hydrate formation appears to increase with the total number of donor and acceptor groups in the molecule.[11] With the imbalance of hydrogen bonding donor and acceptor groups being known to be a driving force for solvate (hydrate) formation, as also seen for **BS**, the ratio of donor : acceptor groups, excluding the water molecules, of the 25 higher hydrate structures was evaluated. Only two structures feature no donor groups (TMAMSU02[72] and YUJJAO[73]) and no structure shows a 1 : 1 ratio or more donor groups than acceptor groups. On average, the hydrate structures, water molecules not considered, show a 1 : 2 ratio, *i.e.* twice the number of acceptor groups than donor groups.

4. Conclusions

The solid-state investigations on brucine sulphate, a compound already mentioned in 1881 (ref. 74) and described as a heptahydrate,[40] revealed that the salt can exist in three different hydrate forms and the amorphous state. The three hydrates seem to be structurally related, explaining the fast transformation kinetics upon changing the RH, but are distinct solid forms exhibiting distinct water contents. Two of the hydrates, **HyA** and **HyC**, show a variable water content depending on the external conditions, *i.e.* relative humidity. The knowledge about the variability of the water content is highly relevant for weighing and dosing operations of a substance and may be critical for adjusting dose uniformity in single unit dosage forms or may lead to substantial errors in any mass based values.[75]

Furthermore, the transformations between the hydrates occur under ambient storage conditions, which involve not only a change in the solid-state form, but also more importantly a substantial change in water content (Fig. 6a). This study revealed that **BS** is practically always associated with water, highlighting the considerable importance of the water molecules for forming and maintaining a stable supramolecular arrangement. This is also confirmed by the fact that the removal of the water (drying at elevated temperature) results in structural collapse.

The study illustrates once again that unravelling the existence of intermediate hydrates, as in the case of **HyB**, or the distinction between stoichiometric, nonstoichiometric and mixed (de)hydration behaviours, requires thorough

investigations with accurate control of the atmospheric conditions.

A complementary study of the incidence of the hydrate formation of organic sulphate salts confirms that salts with this anion are prone to hydration and exist mostly in higher hydration states than other hydrates of organic compounds. The latter can, at least partially, be attributed to the fact that sulphate salts forming higher hydrates tend to show an imbalance in hydrogen bonding donor and acceptor groups. Moreover, through the addition of the water molecules, denser crystal packings are achievable.

Conflicts of interest

There are no conflicts to declare.

Acknowledgements

The author would like to thank Prof. U. J. Griesser (University of Innsbruck) for helpful discussions and Mag. Danya Spechtenhauser for preliminarily work on the compound and gratefully acknowledges funding from the Elise Richter programme of the Austrian Science Fund (FWF, project V436-N34). The calculations have been performed using the HPC infrastructure LEO of the University of Innsbruck.

Notes and references

1 J. Bernstein, *Polymorphism in Molecular Crystals*, Clarendon Press, Oxford, 2002.
2 H. G. Brittain, *Polymorphism in Pharmaceutical Solids*, Informa Healthcare, New York, London, 2009.
3 R. Hilfiker, F. Blatter and M. von Raumer, in *Polymorphism*, ed. R. Hilfiker, 2006, pp. 1–19.
4 C. H. Gu, V. Young, Jr. and D. J. W. Grant, *J. Pharm. Sci.*, 2001, **90**, 1878–1890.
5 J. Bernstein, *Cryst. Growth Des.*, 2011, **11**, 632–650.
6 S. R. Byrn, R. Pfeiffer, M. Ganey, C. Hoiberg and G. Poochikian, *Pharm. Res.*, 1995, **12**, 945–954.
7 A. Y. Lee, D. Erdemir and M. S. Myerson, *Annu. Rev. Chem. Biomol. Eng.*, 2011, **2**, 259–280.
8 C. C. Sun, *J. Pharm. Sci.*, 2009, **98**, 1744–1749.
9 J. Cruz-Cabeza Aurora, M. Reutzel-Edens Susan and J. Bernstein, *Chem. Soc. Rev.*, 2015, **44**, 8619–8635.
10 G. P. Stahly, *Cryst. Growth Des.*, 2007, **7**, 1007–1026.
11 D. E. Braun, *PhD Thesis*, University of Innsbruck, 2008.
12 U. J. Griesser, in *Polymorphism: In the Pharmaceutical Industry*, ed. R. Hilfiker, Wiley-VCH, Germany, 2006, pp. 211–233.
13 S. Gal, *Chimia*, 1968, **22**, 409–425.
14 E. Braun Doris and J. Griesser Ulrich, *Front. Chem.*, 2018, **6**, 31.
15 D. E. Braun and U. J. Griesser, *Cryst. Growth Des.*, 2016, **16**, 6111–6121.
16 F. G. Vogt, J. Brum, L. M. Katrincic, A. Flach, J. M. Socha, R. M. Goodman and R. C. Haltiwanger, *Cryst. Growth Des.*, 2006, **6**, 2333–2354.
17 S. R. Byrn, R. R. Pfeiffer and J. G. Stowell, *Solid-State Chemistry of Drugs*, SSCI, Inc., West Lafayette, Indiana, 2nd edn, 1999.
18 R. K. Khankari and D. J. W. Grant, *Thermochim. Acta*, 1995, **248**, 61–79.
19 H. Zhu, C. Yuen and D. J. W. Grant, *Int. J. Pharm.*, 1996, **135**, 151–160.
20 D. E. Braun, T. Gelbrich, V. Kahlenberg and U. J. Griesser, *Mol. Pharmaceutics*, 2014, **11**, 3145–3163.
21 D. E. Braun, *Phys. Chem. Chem. Phys.*, 2019, **21**, 17288–17305.
22 A. Berzins, T. Rekis and A. Actins, *Cryst. Growth Des.*, 2014, **14**, 3639–3648.
23 D. E. Braun, P. G. Karamertzanis and S. L. Price, *Chem. Commun.*, 2011, **47**, 5443–5445.
24 D. E. Braun and U. J. Griesser, *Cryst. Growth Des.*, 2016, **16**, 6405–6418.
25 A. T. Hulme and S. L. Price, *J. Chem. Theory Comput.*, 2007, **3**, 1597–1608.
26 A. J. Cruz-Cabeza, G. M. Day and W. Jones, *Chem. – Eur. J.*, 2009, **15**, 13033–13040.
27 S. Mohamed, D. P. Karothu and P. Naumov, *Acta Crystallogr., Sect. B: Struct. Sci., Cryst. Eng. Mater.*, 2016, **72**, 551–561.
28 C. Ahlneck and G. Zografi, *Int. J. Pharm.*, 1990, **62**, 87–95.
29 D. E. Braun, L. H. Koztecki, J. A. McMahon, S. L. Price and S. M. Reutzel-Edens, *Mol. Pharmaceutics*, 2015, **12**, 3069–3088.
30 M. D. Eddleston, S. Sivachelvam and W. Jones, *CrystEngComm*, 2013, **15**, 175–181.
31 S. S. Agrawal, S. Saraswati, R. Mathur and M. Pandey, *Life Sci.*, 2011, **89**, 147–158.
32 H. B. Chen, F. S. Ma, J. Q. Fang and F. Fang, *Zhongchengyao*, 2015, **37**, 16–21.
33 X. K. Deng, W. Yin, W. D. Li, F. Z. Yin, X. Y. Lu, X. C. Zhang, Z. C. Hua and B. C. Cai, *J. Ethnopharmacol.*, 2006, **106**, 179–186.
34 W. Yin, X. K. Deng, F. Z. Yin, X. C. Zhang and B. C. Cai, *Food Chem. Toxicol.*, 2007, **45**, 1700–1708.
35 P. S. Rao, M. Ramanadham and M. N. V. Prasad, *Food Chem. Toxicol.*, 2009, **47**, 283–288.
36 R. O. Gould and M. D. Walkinshaw, *J. Am. Chem. Soc.*, 1984, **106**, 7840–7842.
37 G. Quinkert, H. G. Schmalz, E. M. Dzierzynski, G. Duerner and J. W. Bats, *Angew. Chem.*, 1986, **98**, 1023–1024.
38 S. E. Boiadjiev, R. V. Person, G. Puzicha, C. Knobler, E. Maverick, K. N. Trueblood and D. A. Lightner, *J. Am. Chem. Soc.*, 1992, **114**, 10123–10133.
39 F. J. J. Dijksma, R. O. Gould, S. Parsons, P. Taylor and M. D. Walkinshaw, *Chem. Commun.*, 1998, 745–746.
40 P. Groth, Teil 5. Aromatische Kohlenstoffverbindungen mit mehreren Benzolringen heterocyclische Verbindungen, *Chemische Krystallographie*, W. Engelmann, Leipzig, Germany, 1919.
41 A. Bialonska and Z. Ciunik, *Acta Crystallogr., Sect. C: Cryst. Struct. Commun.*, 2004, **60**, o853–o855.

42 A. Bialonska, Z. Ciunik, M. M. Ilczyszyn and M. Siczek, *Cryst. Growth Des.*, 2014, **14**, 6537–6541.
43 G. Smith, U. D. Wermuth and J. M. White, *Acta Crystallogr., Sect. C: Cryst. Struct. Commun.*, 2007, **63**, o489–o492.
44 G. Smith, U. D. Wermuth, P. C. Healy and J. M. White, *Acta Crystallogr., Sect. C: Cryst. Struct. Commun.*, 2006, **62**, o203–o207.
45 T. Watabe, K. Kobayashi, I. Hisaki, N. Tohnai and M. Miyata, *Bull. Chem. Soc. Jpn.*, 2007, **80**, 464–475.
46 S. S. B. Glover, R. O. Gould and M. D. Walkinshaw, *Acta Crystallogr., Sect. C: Cryst. Struct. Commun.*, 1985, **41**, 990–994.
47 A. Bialonska and Z. Ciunik, *Acta Crystallogr., Sect. E: Struct. Rep. Online*, 2005, **61**, o4222–o4224.
48 R. Taylor and P. A. Wood, *Chem. Rev.*, 2019, **119**, 9427–9477.
49 U. J. Griesser and A. Burger, *Int. J. Pharm.*, 1995, **120**, 83–93.
50 A. J. Markvardsen, W. I. F. David, J. C. Johnson and K. Shankland, *Acta Crystallogr., Sect. A: Found. Crystallogr.*, 2001, **57**, 47–54.
51 W. I. F. David, K. Shankland, J. van de Streek, E. Pidcock, W. D. S. Motherwell and J. C. Cole, *J. Appl. Crystallogr.*, 2006, **39**, 910–915.
52 G. S. Pawley, *J. Appl. Crystallogr.*, 1981, **14**, 357–361.
53 A. A. Coelho, *Topas 5*, 2012.
54 H. Martens and T. Naes, *Multivariate Calibration*, Wiley VCH, Chichester, 1991.
55 Y. Roggo, P. Chalus, L. Maurer, C. Lema-Martinez, A. Edmond and N. Jent, *J. Pharm. Biomed. Anal.*, 2007, **44**, 683–700.
56 A. C. Jorgensen, I. Miroshnyk, M. Karjalainen, K. Jouppila, S. Siiria, O. Antikainen and J. Rantanen, *J. Pharm. Sci.*, 2006, **95**, 906–916.
57 M. J. Turner, S. P. Thomas, M. W. Shi, D. Jayatilaka and M. A. Spackman, *Chem. Commun.*, 2015, **51**, 3735–3738.
58 M. J. Turner, S. Grabowsky, D. Jayatilaka and M. A. Spackman, *J. Phys. Chem. Lett.*, 2014, **5**, 4249–4255.
59 C. F. Mackenzie, P. R. Spackman, D. Jayatilaka and M. A. Spackman, *IUCrJ*, 2017, **4**, 575–587.
60 M. J. Frisch, G. W. Trucks, H. B. Schlegel, G. E. Scuseria, J. M. A. Robb, R. Cheeseman, G. Scalmani, V. Barone, B. Mennucci, G. A. Petersson, H. Nakatsuji, M. Caricato, X. Li, H. P. Hratchian, A. F. Izmaylov, J. Bloino, G. Zheng, J. L. Sonnenberg, M. Hada, M. Ehara, K. Toyota, R. Fukuda, J. Hasegawa, M. Ishida, T. Nakajima, Y. Honda, O. Kitao, H. Nakai, T. Vreven, J. A. Montgomery, J. E. Peralta, F. Ogliaro, M. Bearpark, J. J. Heyd, E. Brothers, K. N. Kudin, V. N. Staroverov, R. Kobayashi, J. Normand, K. Raghavachari, A. Rendell, J. C. Burant, S. S. Iyengar, J. Tomasi, M. Cossi, N. Rega, J. M. Millam, M. Klene, J. E. Knox, J. B. Cross, V. Bakken, C. Adamo, J. Jaramillo, R. Gomperts, R. E. Stratmann, O. Yazyev, A. J. Austin, R. Cammi, C. Pomelli, J. W. Ochterski, R. L. Martin, K. Morokuma, V. G. Zakrzewski, G. A. Voth, P. Salvador, J. J. Dannenberg, S. Dapprich, A. D. Daniels, O. Farkas, J. B. Foresman, J. V. Ortiz, J. Cioslowski and D. J. Fox, *Gaussian 09*, Gaussian Inc., Wallingford, CT, 2009.
61 S. J. Clark, M. D. Segall, C. J. Pickard, P. J. Hasnip, M. J. Probert, K. Refson and M. C. Payne, *Z. Kristallogr.*, 2005, **220**, 567–570.
62 J. P. Perdew, K. Burke and M. Ernzerhof, *Phys. Rev. Lett.*, 1996, **77**, 3865–3868.
63 D. Vanderbilt, *Phys. Rev. B*, 1990, **41**, 7892–7895.
64 A. Tkatchenko and M. Scheffler, *Phys. Rev. Lett.*, 2009, **102**, 073005.
65 S. Grimme, *J. Comput. Chem.*, 2006, **27**, 1787–1799.
66 A. L. Spek, *Acta Crystallogr., Sect. D: Biol. Crystallogr.*, 2009, **65**, 148–155.
67 D. E. Braun, J. A. McMahon, R. M. Bhardwaj, J. Nyman, M. A. Neumann, J. van de Streek and S. M. Reutzel-Edens, *Cryst. Growth Des.*, 2019, **19**, 2947–2962.
68 H. D. Clarke, K. K. Arora, H. Bass, P. Kavuru, T. T. Ong, T. Pujari, L. Wojtas and M. J. Zaworotko, *Cryst. Growth Des.*, 2010, **10**, 2152–2167.
69 H. G. Brittain, K. R. Morris and S. X. M. Boerrigter, in *Polymorphism in Pharmaceutical Solids*, 2nd edn, 2009, pp. 233–281.
70 J. van de Streek and S. Motherwell, *CrystEngComm*, 2007, **9**, 55–64.
71 U. J. Griesser and D. E. Braun, Crystal Polymorphism in Pharmaceuticals: A Statistical Approach, Duesseldorf: PhandTA9.
72 M. G. Wenzel, P. A. Gale and M. E. Light, 2011, CSD Communication.
73 B. M. Kariuki and W. Jones, *Acta Crystallogr., Sect. C: Cryst. Struct. Commun.*, 1995, **51**, 1234–1240.
74 W. A. Shenstone, *J. Chem. Soc., Trans.*, 1881, **39**, 453–462.
75 M. Reutzel-Edens Susan, E. Braun Doris and W. Newman Ann, in *Polymorphism in the Pharmaceutical Industry: Solid Form and Drug Development*, ed. R. Hilfiker and M. Von Raumer, Wiley-VCH, 2019, vol. 2, pp. 159–188.

